

---

# Single-phase deep learning in cortico-cortical networks

---

**Will Greedy\***

Bristol Computational Neuroscience Unit  
Department of Computer Science, SCEEM  
University of Bristol, United Kingdom  
will.greedy@bristol.ac.uk

**Heng Wei Zhu\***

Bristol Computational Neuroscience Unit  
School of Phys., Pharm. and Neuroscience  
University of Bristol, United Kingdom  
hengwei.zhu@bristol.ac.uk

**Joseph Pemberton**

Bristol Computational Neuroscience Unit  
Department of Computer Science, SCEEM  
University of Bristol, United Kingdom  
oq19042@bristol.ac.uk

**Jack Mellor**

School of Phys., Pharm. and Neuroscience  
University of Bristol, United Kingdom  
jack.mellor@bristol.ac.uk

**Rui Ponte Costa**

Bristol Computational Neuroscience Unit  
Department of Computer Science, SCEEM  
University of Bristol, United Kingdom  
rui.costa@bristol.ac.uk

## Abstract

The error-backpropagation (backprop) algorithm remains the most common solution to the credit assignment problem in artificial neural networks. In neuroscience, it is unclear whether the brain could adopt a similar strategy to correctly modify its synapses. Recent models have attempted to bridge this gap while being consistent with a range of experimental observations. However, these models are either unable to effectively backpropagate error signals across multiple layers or require a multi-phase learning process, neither of which are reminiscent of learning in the brain. Here, we introduce a new model, bursting cortico-cortical networks (BurstCCN), which solves these issues by integrating known properties of cortical networks namely bursting activity, short-term plasticity (STP) and dendrite-targeting interneurons. BurstCCN relies on burst multiplexing via connection-type-specific STP to propagate backprop-like error signals within deep cortical networks. These error signals are encoded at distal dendrites and induce burst-dependent plasticity as a result of excitatory-inhibitory topdown inputs. First, we demonstrate that our model can effectively backpropagate errors through multiple layers using a single-phase learning process. Next, we show both empirically and analytically that learning in our model approximates backprop-derived gradients. Finally, we demonstrate that our model is capable of learning complex image classification tasks (MNIST and CIFAR-10). Overall, our results suggest that cortical features across sub-cellular, cellular, microcircuit and systems levels jointly underlie single-phase efficient deep learning in the brain.

---

\*Equal contributions

# 1 Introduction

For effective learning, synaptic modifications throughout the brain should result in improved behavioural function. This requires a process by which credit should be assigned to synapses given their contribution to behavioural output [1–3]. In multilayer networks, credit assignment is particularly challenging as the impact of changing a synaptic connection depends on its downstream brain areas. Classical local Hebbian plasticity rules, even when coupled with global neuromodulatory factors, are unable to communicate enough information for effective credit assignment through multiple layers of processing [3]. In machine learning, the error-backpropagation (backprop) algorithm is the most successful solution to the credit assignment problem. However, it relies on a number of biologically implausible assumptions to compute gradient information used for synaptic updates. Previous work has attempted to address these implausibilities but important issues remain open in terms of mapping backprop to the neuronal physiology. Earlier attempts relied on mapping backprop to the brain by using single-compartment neuron models [4, 5]. This poses a problem as single-compartment neurons are unable to simultaneously store the necessary inference and credit assignment signals. One solution is to model neurons with an apical dendritic compartment that separately stores credit information [5, 6], supported by the electrotonic separation of the soma and apical dendrites [7]. These distal credit signals can then be communicated to the soma through non-linear dendritic events that trigger bursting at the soma [8], thereby inducing long-term synaptic plasticity [9]. In particular, two recent approaches, Error-encoding Dendritic Networks (EDNs) [6] and Burstprop [10], have demonstrated how such multi-compartment neuron models can be used to construct networks capable of backprop-like credit assignment. EDNs encode credit signals at apical dendrites resulting from the mismatch between dendritic-targeting interneuron activity and downstream activity. Burstprop uses the mechanism of bursting, controlled by dendritic excitability, to communicate credit signals. However, these models still have major issues, such as the inability to effectively backpropagate error signals through many layers (EDNs) and the requirement for a multi-phase learning process (Burstprop).

Here, we propose a new model called the Bursting Cortico-Cortical Network (BurstCCN) as a solution to the credit assignment problem which addresses several outstanding issues of current biologically plausible backprop research. Our model builds upon prior multi-compartment neuron models [6, 10]: it encodes credit signals in distal dendritic compartments which trigger bursting activity at the somatic level to drive backprop-like synaptic updates. We demonstrate that combining well-established properties of cortical neurons such as bursting activity, short-term plasticity (STP) and dendrite-targeting interneurons provides a biologically plausible mechanism for performing credit assignment. In contrast to previous models, BurstCCN is highly effective at backpropagating credit signals in multi-layer architectures while only requiring a single-phase learning process. We implement multiple versions of the BurstCCN at different levels of abstraction in order to demonstrate some of its key properties and empirically confirm our theoretically motivated claims.

First, we used a spike-based implementation of the BurstCCN to demonstrate its ability to learn without the need for multiple phases. We further show the importance of this single-phase learning by training a continuous-time rate-based version of the BurstCCN on a continuous-time non-linear regression task. Next, we show empirically and analytically that our model’s dynamics result in learning that approximately follows backprop-derived gradients. Finally, we use a simplified discrete-time BurstCCN implementation to demonstrate that the model achieves good performance in non-trivial image classification tasks (MNIST and CIFAR-10), even in the presence of random feedback synaptic weights.

## 2 Bursting Cortico-Cortical Networks

### 2.1 Burst Ensemble Multiplexing

Burst Ensemble Multiplexing (BEM) [11] refers to the idea that ensembles of cortical neurons are capable of simultaneously representing multiple distinct signals within the patterns of their spiking activity. Typically, pyramidal cells receive top-down and bottom-up signals into their apical and basal dendrites, respectively. Bottom-up basal inputs affect the rate of spiking and top-down apical inputs convert these somatically induced spikes into high-frequency bursts. Postsynaptic populations can then use STP to decode these distinct signals from the overall spiking activity.

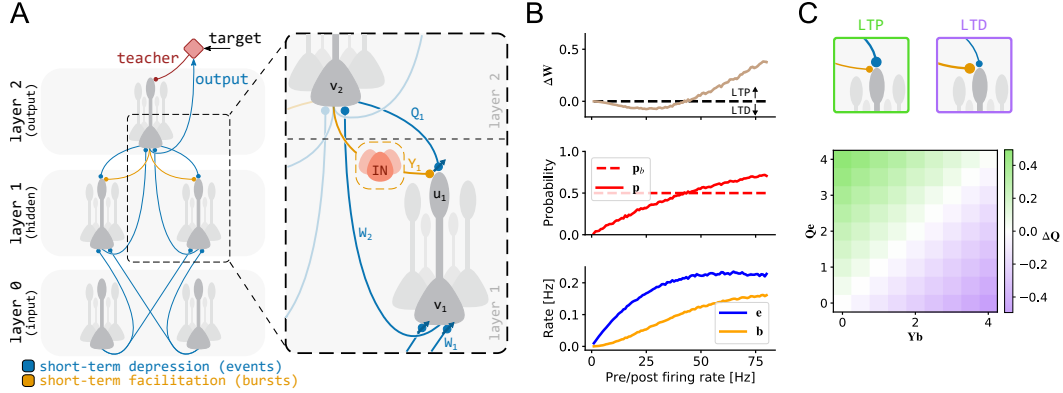


**Figure 1: Bursting cortico-cortical networks (BurstCCN) for credit assignment through bursting activity.** (A) Schematic of network with neuron ensembles and STP-specific connection types. Events from the input are propagated forward through short-term depressing (STD) connections,  $\mathbf{W}$ . Output event rates are compared to a target value which generates a teaching signal presented to the output layer apical dendrites. This acts as an error signal and appears as a deflection in the dendritic potential from its resting potential which causes changes to bursting activity from its baseline. The error-carrying bursting signals are propagated back through short-term facilitating connections,  $\mathbf{Y}$ , which we interpret as being communicated by populations of dendrite-targeting interneurons. Events are also propagated backwards via STD connections,  $\mathbf{Q}$ , to provide a means of cancelling baseline bursting activity. The difference in activity from these two feedback connections results in changes to dendritic excitability that lead to burst-dependent synaptic plasticity. (B) Burst-dependent plasticity rule. Simple setup of a single connection between a pre- and post-synaptic cell that are both modelled with Poisson spike trains with equal rates. As the firing rates increase, (top) plasticity of the synaptic weight switches from long-term depression (LTD) to long-term potentiation (LTP) (middle) when the burst probability increases above the baseline value. (Bottom) The magnitude of the weight change is scaled by the event rate. (C) Homeostatic plasticity rule for  $\mathbf{Q}$  weights. Difference between the signal through  $\mathbf{Q}$  and  $\mathbf{Y}$  dictates the direction and magnitude of synaptic plasticity.

The BurstCCN uses the concept of BEM in a similar way to Burstprop [10] in which ensembles of cells encode both feedforward inference signals and feedback error signals. The model encodes these signals as the rates of *events* and *bursts*, respectively, across the ensembles. Here, the specific definition of a burst is a collection of spikes with interspike intervals less than 16ms and an event is either a burst or a single isolated spike (i.e. a spike not followed or preceded by another within 16ms). The burst probability of an ensemble is defined as the probability that an event at a given time is a burst and is computed as a ratio of the event rate ( $e$ ) and burst rate ( $b$ ):  $p = b/e$ .

## 2.2 Rate-based BurstCCN

In our discrete-time implementation of the rate-based BurstCCN, example input-output pairs are processed independently in discrete timesteps. For each example, the event rates of the input layer,  $\mathbf{e}_0$ , encode the input stimulus. The model then computes each subsequent layer's activities, equivalent to that of a standard feedforward artificial neural network (Fig. 1A). Specifically, somatic potentials are computed by integrating basal input as  $\mathbf{v}_l = \mathbf{W}_l \mathbf{e}_{l-1}$  where  $\mathbf{W}_l$  are short-term depressing (STD) feedforward weights from layer  $l - 1$  to layer  $l$ . The STD nature of these weights ensures that only event rate information propagates forwards. Each layer's event rates are then computed by applying a non-linear activation function,  $f$ , to the somatic potentials,  $\mathbf{e}_l = f(\mathbf{v}_l)$ . These linear and nonlinear operations are repeated for each layer in the network to ultimately obtain the output layer event rates,  $\mathbf{e}_L$ , where  $L$  denotes the total number of layers.

The desired target output of the network,  $\mathbf{e}_{target}$ , is compared to the output layer event rates to produce a signed error,  $\mathbf{e}_{target} - \mathbf{e}_L$ , which is used as a teaching signal. This error information is then propagated backwards through each layer in the network by altering the apical dendritic compartment potential and, as a result, the burst probability of each pyramidal ensemble. At the output layer, the burst probability is computed directly as  $\mathbf{p}_L = \mathbf{p}_L^b + \mathbf{p}_L^b \odot (\mathbf{e}_{target} - \mathbf{e}_L) \odot h(\mathbf{e}_L)$  where  $\odot$  denotes

the element-wise product,  $\mathbf{p}_L^b$  represents the baseline burst probability in the absence of any teaching signal and  $h(\mathbf{e}_l) = f'(\mathbf{v}_l) \odot \mathbf{e}_l^{-1}$ . These burst probabilities are used at the output layer ( $l = L$ ) to compute the burst rates as  $\mathbf{b}_l = \mathbf{e}_l \odot \mathbf{p}_l$  which are decoded and sent backwards to layer  $l - 1$  apical dendrites by a set of short-term facilitating (STF) feedback weights,  $\mathbf{Y}_{l-1}$ . The event rates are also sent backwards through a separate set of STD feedback weights,  $\mathbf{Q}_{l-1}$ , leading to an apical dendritic potential in the previous layer of  $\mathbf{u}_{l-1} = \mathbf{Q}_{l-1}\mathbf{e}_l - \mathbf{Y}_{l-1}\mathbf{b}_l$ . This determines the layer's burst probabilities which are computed as  $\mathbf{p}_{l-1} = \bar{\sigma}(\mathbf{u}_{l-1} \odot h(\mathbf{e}_{l-1}))$  where  $\bar{\sigma}$  denotes the sigmoid function,  $\sigma$ , with scaling and offset parameters,  $\bar{\sigma}(x) = \sigma(\alpha x + \beta)$  ([10]; see SM, Section B.1). The same process is repeated backwards for each layer until the input layer to obtain their dendritic potentials and burst probabilities. We interpret the STF feedback connections as being provided via a type of dendrite-targeting interneuron and STD feedback as direct connections in line with recent experimental studies [12–17].

After the error information has been propagated backwards, feedforward synaptic weight changes are computed using a burst-dependent synaptic plasticity rule:

$$\Delta \mathbf{W}_l = \eta_l^{(\mathbf{W})} ((\mathbf{p}_l - \mathbf{p}_l^b) \odot \mathbf{e}_l) \mathbf{e}_{l-1}^T \quad (1)$$

where  $\eta_l^{(\mathbf{W})}$  is a learning rate and  $T$  is the transpose operation. Importantly, the learning rule depends on the change in burst probability from the predefined layer-wise baseline burst probability,  $\mathbf{p}_l^b = p_l^b(1, \dots, 1)^T$ , which represents the signed error signal required for backprop-like learning. Consequently, when we make both pre- and postsynaptic cells fire following Poisson statistics we obtain long-term depression and long-term potentiation for low and high firing rates, respectively (Fig. 1B). This is in line with a large number of experimental studies at cortical synapses [18, 19]. It can be shown that the updates produced by this learning rule approximate those obtained by the backpropagation algorithm in the weak-feedback case (see Section 3.3.1 and SM, Section B).

In the absence of a teaching signal, it is important for pyramidal ensembles to produce a baseline level of bursting such that no weight changes occur (cf. Eq. 1). This holds true for the output layer as there are no other inputs onto the apical dendrites. However, for the hidden layers the event rate signals through  $\mathbf{Q}$  and the burst rate signals through  $\mathbf{Y}$  need to exactly cancel each other out such that the apical dendritic potentials are at rest (i.e.  $\mathbf{u} = 0$ ). For any  $\mathbf{Y}$  weights, there is always an optimal set of  $\mathbf{Q}$  weights that will produce this exact cancellation regardless of the event rates propagating through the network. Specifically, they must be set as  $\mathbf{Q}_l = p_l^b \mathbf{Y}_l$  which we refer to as the weights being in a *Q-Y symmetric* state. As it is not biologically plausible for the  $\mathbf{Q}$  synapses to have direct knowledge of  $\mathbf{Y}$ , inspired by earlier work [6, 20] we use a learning rule for  $\mathbf{Q}$  that provides this cancellation:

$$\Delta \mathbf{Q}_l = -\eta_l^{(\mathbf{Q})} \mathbf{u}_l \mathbf{e}_{l+1}^T \quad (2)$$

which explicitly aims to silence the apical potentials (Fig. 1C). In the absence of a teaching signal at the output layer, all  $\mathbf{Q}$  weights will eventually converge to their optimal values and achieve a symmetric state (i.e.  $\mathbf{u} = 0$ ) under reasonable assumptions (see SM, Section B.2). Note that we could similarly have added this learning rule on the  $\mathbf{Y}$  feedback weights to cancel the  $\mathbf{Q}$  weights, which produces similar results (Fig. S1).

When teaching signals are applied at the output layer, it is important to note that only the bursting activity propagated through the  $\mathbf{Y}$  connections changes because the event rates through  $\mathbf{Q}$  are unaffected by the dendritic activity. This enables single-phase learning as the symmetry in the two feedback connection types ( $\mathbf{Q}$  and  $\mathbf{Y}$ ) can be exploited to directly compare *without teacher* signals (i.e. at baseline) to *with teacher* signals.

Details of the continuous time implementation can be found in the Supplementary Materials.

### 2.3 Spiking BurstCCN

For a spiking implementation of BurstCCN, we adapted our burst-dependent synaptic plasticity rule in Equation 1 (see SM, Eq. 12). Unlike the two rate-based implementations, the spiking BurstCCN more accurately models the internal neuron spiking dynamics instead of abstracting these details away and only considering the ensemble-level behaviour. Neurons are modelled with two compartments corresponding to the soma and apical dendrites and spikes are generated when a somatic threshold potential is met (see Section A.2 for more details).

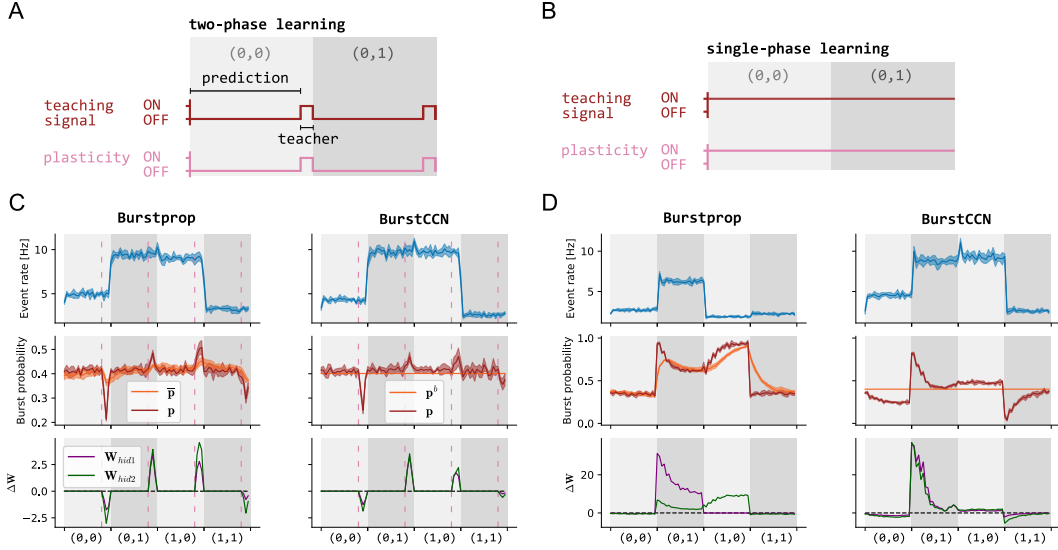


**Figure 2: Spiking BurstCCN does not require multi-phase learning to solve the XOR classification task.** Schematic of the (A) two-phase and (B) single-phase learning settings. (A) For each input during two-phase learning, networks are given a 7.2s prediction period during which teaching signals and plasticity are turned OFF, followed by a 0.8s learning period where both teaching signals and plasticity remained ON throughout training. (B) During single-phase learning, both the teaching signals and plasticity remained ON throughout training. (C, D) Top: event rate ( $e$ ) of the output layer; Middle: burst probability ( $p$ ) for the output layer and the baseline or moving average of the burst probability ( $p^b$  or  $\bar{p}$ ) for BurstCCN and Burstprop, respectively; Bottom: the resulting weight updates for connections from hidden layer neurons. Model results represent mean  $\pm$  standard error ( $n = 5$ ).

## 3 Results

### 3.1 BurstCCN can learn with a single learning phase

A key motivation for developing the BurstCCN was to design a model capable of learning without the need for separate learning phases, while being consistent with a range of cortical features across multiple levels. To demonstrate that our model can perform single-phase learning, we trained the spiking version of our model on the XOR classification task and contrasted it with Burstprop, which requires a two-phase learning process (Fig. 2). In both single- and two-phase learning regimes, the input stimulus is presented for a total of 8s before the next example is shown. The two-phase learning regime has an initial prediction phase, lasting 7.2s for each input presentation, where plasticity is switched off throughout the network and the output neurons do not receive any teaching signals (Fig. 2A). This is followed by a teacher phase for the remaining 0.8s where plasticity is restored and teaching signals are delivered at the output. The single-phase regime removes the initial prediction phase and extends the teacher phase to the full duration of the input stimulus (Fig. 2B).

Our results show that both models were capable of successfully learning the task in the two-phase regime as indicated by the high output event rates in response to the  $(0, 1)$  and  $(1, 0)$  inputs and low event rates for the  $(0, 0)$  and  $(1, 1)$  inputs (Fig. 2C). However, when training in the single-phase regime, only BurstCCN was able to learn the task (Fig. 2D). The inability of Burstprop to learn the task can be explained by comparing the moving average of the burst probability ( $\bar{p}$ ) with the actual burst probability ( $p$ ) which determines the sign of synaptic weight updates (Fig. 2D). Burstprop failed to learn in the single-phase learning setup due to the need to have a stable representation of  $\bar{p}$  without a teaching signal, which becomes problematic in this case.

### 3.2 BurstCCN can learn with dynamic input-output

Typically, studies that have attempted to solve the credit assignment problem with biologically plausible implementations of backprop make an implicit assumption that during learning there is

a period where the continuous-time input stream is fixed [6, 10]. This is required in most cases to allow the network to stabilise its activities before learning can take place. With single-phase learning, we can relax this assumption which enables learning in conditions where the inputs and their corresponding teaching signals are dynamically changing over time. We assessed this ability by training the continuous-time BurstCCN (see SM, Section A.1) on an online non-linear regression task (Fig. 3). This task consisted of three sinusoidal inputs,  $x_i = \sin(\alpha_i t + \beta_i)$ , with random frequencies  $\alpha_i \sim U(0, \frac{\pi}{2})$  and phase offsets  $\beta_i \sim U(0, 2\pi)$  (Fig. 3A). The network had a single output unit for which a non-trivial target was obtained by passing the same inputs to a 3-25-1 artificial neural network (ANN). This approximates a setting in which a given cortical area learns to regress its input onto the activity of another cortical area. The ANN weights were randomly initialised with  $w_{ij}^1 \sim \mathcal{U}(-\sqrt{3}, \sqrt{3})$  for the first layer and  $w_{ij}^2 \sim \mathcal{U}(-0.6, 0.6)$  for the second layer. Despite the BurstCCN initially producing outputs that were significantly different to the target (Fig. 3C), the results showed that over training it learned to produce output patterns that closely matched the non-linear and dynamic target (Fig. 3B,D). This highlights that the BurstCCN is capable of adequately backpropagating useful error signals when both inputs and teaching signals are constantly changing.

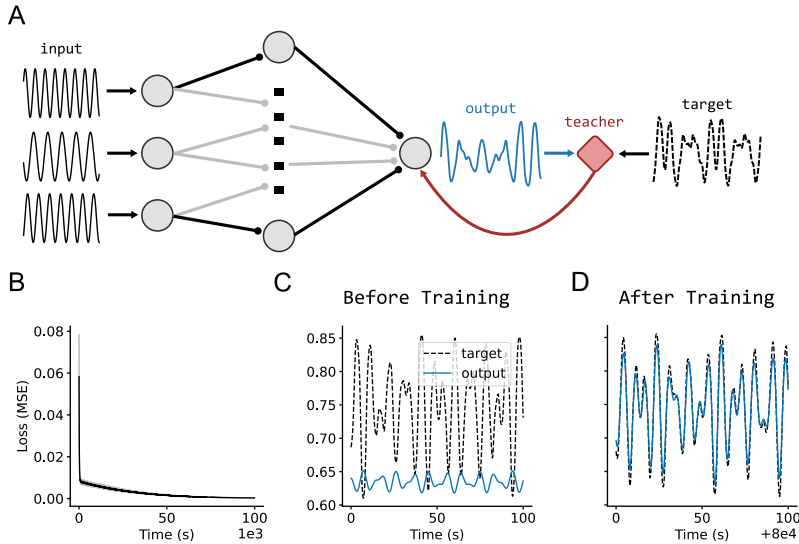


Figure 3: **BurstCCN can learn a dynamic non-linear regression task.** (A) Schematic of the task. Three sinusoidal waves with random frequencies are given as inputs. The network needs to learn to match the target pattern which is obtained by passing the same inputs through a fixed, randomly initialised ANN. (B) Learning curve for the (continuous-time) BurstCCN. (C, D) Example output traces for (C) before and (D) after training. Model results represent mean  $\pm$  standard error ( $n = 5$ ).

### 3.3 Feedback plasticity rule facilitates alignment to backprop updates

Next, we wanted to understand how well our model approximates backprop. As stated above, the purpose of the learning rule for the feedback **Q** STD connections (Eq. 2) is to silence the apical compartment of every ensemble by cancelling activity through the feedback **Y** STF connections. When a teaching signal is applied, this becomes important for computing the correct local error signal that is used for learning and backpropagated to previous layers. Here we show analytically and empirically using the discrete version of the model how the errors computed by our model relate to backprop.

#### 3.3.1 BurstCCN with weak feedback approximates backpropagation algorithm

With some small assumptions, it can be shown analytically that the weight update term defined in Equation 1 approximates true error backpropagation; that is,  $\Delta w_{ij} \approx -\frac{\partial E^{\text{task}}}{\partial w_{ij}}$  where  $E^{\text{task}} = \|\mathbf{e}_L - \mathbf{e}_{\text{target}}\|^2$  is the task error defined at the last layer. In particular, if we focus on the change in burst rate  $\delta \mathbf{b}_l := (\mathbf{p}_l - \mathbf{p}_l^b) \odot \mathbf{e}_l$  (as in right hand side of Eq. 1) and assume that the feedback

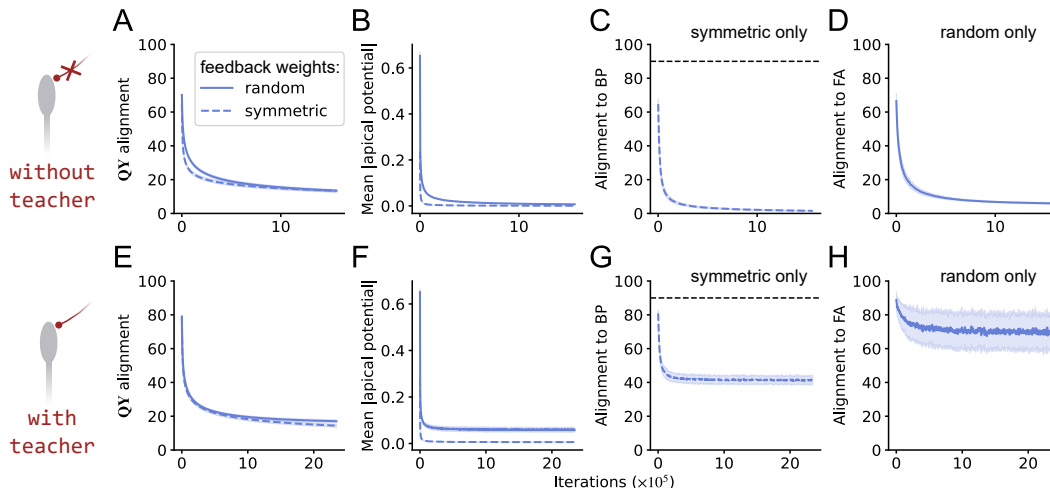


Figure 4: **Feedback learning rule enables a close alignment with backprop and feedback alignment.** The network is a randomly initialised 5-layer discrete-time BurstCCN with random (solid line) or symmetric (dashed line), fixed  $\mathbf{W}$  and  $\mathbf{Y}$  weights. The  $\mathbf{Q}$  weights are updated in the presence of (A-D) no teaching signal or (E-H) a teaching signal. (A,E) Alignment between  $\mathbf{Q}$  and  $\mathbf{Y}$  connections, (B,F) the mean absolute value of the apical potentials, (C,G) the alignment to backprop (BP) and (D,H) feedback alignment (FA) as  $\mathbf{Q}$  weights learn to silence apical dendrite potential. Updates below  $90^\circ$  marked by the black dashed line are considered useful as they still follow the direction to backprop on average. Model results represent mean  $\pm$  standard error ( $n = 5$ ).

weights are optimally aligned, i.e.  $\mathbf{Q}_l = p_l^b \mathbf{Y}_l$ , we can derive the following iterative relationship:

$$\delta \mathbf{b}_l = f'(\mathbf{v}_l) \odot (-\mathbf{Y}_l) \delta \mathbf{b}_{l+1} + \mathcal{O}(\mathbf{u}_l^3) \quad (3)$$

Since  $\delta \mathbf{b}_L = -\frac{\partial E^{\text{task}}}{\partial \mathbf{v}_L}$  (by construction), Equation 3 thus replicates the backpropagation of error algorithm to a third order<sup>2</sup> approximation with respect to the apical potentials  $\mathbf{u}_l$  when the feedforward and feedback weights are perfectly aligned,  $\mathbf{Y}_l = -\mathbf{W}_{l+1}^T$ . We refer to this as the *W-Y symmetric* state. Applying the chain rule  $\frac{\partial E^{\text{task}}}{\partial \mathbf{W}_l} = \frac{\partial E^{\text{task}}}{\partial \mathbf{v}_l} \left( \frac{\partial \mathbf{v}_l}{\partial \mathbf{W}_l} \right)^T$  and noting that  $\frac{\partial \mathbf{v}_l}{\partial \mathbf{W}_l} = \mathbf{e}_{l-1}$ , the link between the weight update defined in Equation 1 to that used in error backpropagation then becomes clear:

$$\Delta \mathbf{W}_l^{\text{BurstCCN}} = \eta_l^{(\mathbf{W})} \delta \mathbf{b}_l \mathbf{e}_{l-1}^T \quad (4)$$

$$\Delta \mathbf{W}_l^{\text{backprop}} = -\eta_l^{(\mathbf{W})} \frac{\partial E^{\text{task}}}{\partial \mathbf{v}_l} \mathbf{e}_{l-1}^T \quad (5)$$

To approach an equivalence to backpropagation, however, it remains to show that the apical potentials  $\mathbf{u}_l$  are indeed appropriately small (so that  $\|\mathbf{u}_l^3\| \rightarrow 0$  in Equation 3) for each layer  $l$ , which can be shown by induction. Assuming that the apical potentials of the above layer  $\mathbf{u}_{l+1}$  are small, we can derive the recursive relationship  $\mathbf{u}_l \approx f'(\mathbf{v}_{l+1}) \odot (-\mathbf{Y}_l) \mathbf{u}_{l+1}$ . This then highlights that if the derivative of the activation function  $f'$  is bounded by 1 (as is true for sigmoid and most activation functions) and the feedback weights  $\mathbf{Y}_l$  are reasonably small, then we have  $\|\mathbf{u}_l\| \leq \|\mathbf{u}_{l+1}\|$  (see SM, Section B, for full derivation). Therefore, if the original error gradient defined at the last layer  $\frac{\partial E^{\text{task}}}{\partial \mathbf{e}_N}$  (and therefore  $\mathbf{u}_{L-1}$ ) is appropriately small, our condition that  $\mathbf{u}_l$  is small for each layer  $l$  is satisfied and  $\Delta \mathbf{W}_l^{\text{BurstCCN}} \approx \Delta \mathbf{W}_l^{\text{backprop}}$ .

### 3.3.2 Learning $\mathbf{Q}$ feedback connections better approximates backprop-derived gradients

We empirically evaluated our feedback plasticity rule by updating *only* the  $\mathbf{Q}$  weights of a randomly initialised 5-layer discrete-time BurstCCN with all other weight types ( $\mathbf{W}$  and  $\mathbf{Y}$ ) fixed. We used

<sup>2</sup>Here we use abuse of notation  $\mathbf{u}_l^3 = (u_{l,1}^3, u_{l,2}^3, \dots)^T$  to represent the element-wise cubic of  $\mathbf{u}_l$

multiple initialisations and training regimes to understand how the plasticity rule behaves in different scenarios. The network was either initialised in the  $\mathbf{W}$ - $\mathbf{Y}$  symmetric state or with random feedback weights (where  $\mathbf{Y}_l \neq -\mathbf{W}_{l+1}^T$ ). We computed the angle between the update calculated from the feedforward plasticity rule (Eq. 1) and either backprop or feedback alignment [4] for the symmetric and random configurations, respectively. We examined both cases: in the theoretically ideal case for learning  $\mathbf{Q}$ , where no teaching signal is present (Fig. 4A-D), and with a teaching signal at the output layer (Fig. 4E-H).

In all cases, as the alignment between the  $\mathbf{Q}$  and  $\mathbf{Y}$  connections improved (Fig. 4A,E), the apical potential decreased (Fig. 4B,F) and this resulted in updates that more closely aligned to backprop (Fig. 4C,G) and feedback alignment (Fig. 4D,H). In the absence of a teaching signal, this alignment angle to both backprop and feedback alignment eventually became very small which shows that the model approximates backprop updates supporting our analytical results (Fig. 4C-D). Despite producing less aligned feedforward updates in the presence of a teaching signal, the updates computed were still informative since they were consistently well below  $90^\circ$  of the direction of steepest descent (Fig. 4G).

### 3.4 BurstCCN learns image classification tasks with multiple hidden layers

#### 3.4.1 MNIST

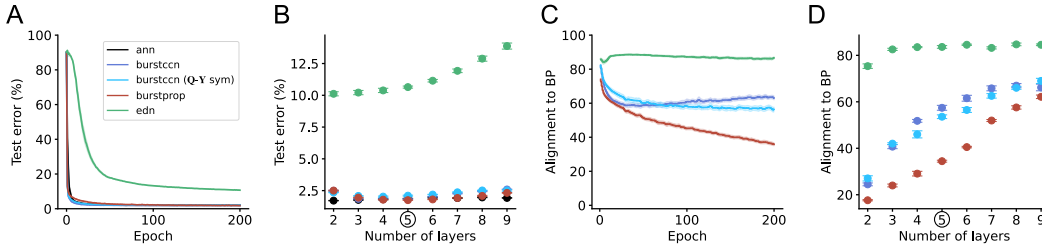


Figure 5: **BurstCCN learns to classify handwritten digits (MNIST) with deep networks.** (A) Learning curve and (C) alignment to backprop of 5-layer BurstCCN (blue), BurstCCN ( $\eta^{(\mathbf{Q})} = 0$ ) (light blue), Burstprop (red) and EDN (green). (B) Different number of hidden layers across all models. (D) Alignment to backprop (BP) across number of hidden layers. The black circle indicates that the hyperparameters for each model were optimised for 5-layer networks. Model results represent mean  $\pm$  standard error ( $n = 5$ ).

Next, to test whether our model can indeed perform backprop-like deep learning, we trained a number of (discrete-time) BurstCCN architectures on the MNIST handwritten digit classification task [21]. We compared the BurstCCN with Burstprop [10] and EDNs [6] using similar architectures (see SM, Section C.3.3). We focus on the more biologically plausible case of using random fixed feedback weights (i.e. feedback alignment [4]; see Fig. S2 for symmetric feedback weight case) with the remaining connection types updated using their own plasticity rules as given by the different models. To be able to test our model in its idealised case we also tested a model for which the feedback STD weights ( $\mathbf{Q}$ ) were fixed in the  $\mathbf{Q}$ - $\mathbf{Y}$  symmetric state (see Section 2.2), we denote this model as "BurstCCN ( $\mathbf{Q}$ - $\mathbf{Y}$  sym)".

Using 5-layer networks, the BurstCCN obtained a test error of  $1.84 \pm 0.01\%$ , comparable to that of Burstprop with  $1.75 \pm 0.01\%$  and significantly outperforming the EDN with  $10.65 \pm 0.09\%$  (Fig. 5A). As the network depth increased, both BurstCCN and Burstprop retained high performances but the EDN showed a substantial decay in performance with deeper networks (Fig. 5B). In an idealised case for the EDN, the disparity in performance and the effect of depth is less evident (Fig. S3). We then compared the alignment between the models and backprop. For the 5-layer networks, Burstprop's updates were most closely aligned to backprop, followed by the two BurstCCN models which all vastly outperformed the EDN (Fig. 5C). As expected, the BurstCCN with  $\mathbf{Q}$ - $\mathbf{Y}$  symmetry could better propagate error signals. By increasing the network depth, we demonstrate that it was more difficult to produce updates that were closely aligned to backprop. However, we show that the BurstCCN was still capable of backpropagating useful error signals in relatively deep networks (Fig. 5D).



### 3.4.2 CIFAR-10

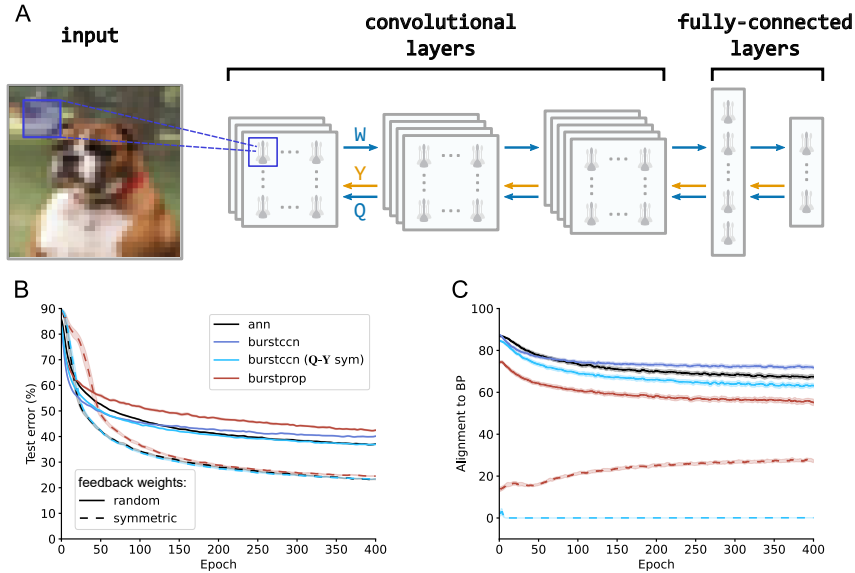


Figure 6: **BurstCCN with convolutional layers learns to solve natural image classification task (CIFAR-10).** (A) Schematic of networks trained consisting of an input layer, three convolutional layers, a fully-connected hidden layer and output layer. For the BurstCCN, each layer was connected with a set of feedforward weights,  $W$ , and feedback weights,  $Y$  and  $Q$  (see main text for details). (B) Learning curve and (C) alignment to backprop of the different models with random (solid lines) and symmetric (dashed lines) feedback weight regimes. Model results represent mean  $\pm$  standard error ( $n = 5$ ).

Finally, we investigated the capabilities of the BurstCCN on more challenging tasks that are commonly tested in deep learning. We constructed a deep network consisting of three convolutional layers followed by a fully-connected hidden layer and output layer (Fig. 6A). We trained BurstCCN and Burstprop models using this network architecture on the CIFAR-10 image classification task [22]. BurstCCN ( $Q$ - $Y$  sym) was trained in the  $Q$ - $Y$  symmetric regime whereas BurstCCN was initialised in this state and  $Q$  weights were then updated using the corresponding plasticity rule. All model types were tested with two feedback weight regimes:  $W$ - $Y$  symmetric and random fixed  $Y$  feedback weights (i.e. feedback alignment).

After training, we observed a test error of  $38.99 \pm 0.18\%$  for BurstCCN with random feedback weights, similar to performances achieved by feedback alignment with an ANN ( $36.30 \pm 0.16\%$ ) and Burstprop ( $41.32 \pm 0.14\%$ ) (Fig. 6B). For the  $W$ - $Y$  symmetric regime which most resembles backprop, BurstCCN ( $22.92 \pm 0.03\%$ ) performed significantly better than all feedback alignment setups and, once again, obtained a similar error to the symmetric ANN ( $22.62 \pm 0.10\%$ ) and Burstprop ( $24.15 \pm 0.17\%$ ) cases. The increased performance seen in the symmetric setups can be explained by the improvement in alignment to backprop updates (Fig. 6C).

## 4 Conclusions and discussion

We introduced a new model capable of backprop-like credit assignment by integrating known properties of cortical networks. We have shown that by combining specific biological mechanisms such as bursting, STP and dendrite-targeting inhibition it is possible to construct a model that learns effectively in a continuous setting that is reminiscent of learning in the brain. Moreover, we have demonstrated that such a model can learn complex image classification tasks in deep networks.

Our model proposes specific STP dynamics on the feedforward and feedback connections. It requires STD on cortico-cortical projections onto pyramidal cells in line with experimental evidence [12–16]. In addition, it suggests a key role for dendrite-targeting interneurons such as SST-positive Martinotti cells in the feedback pathway. There is evidence that these interneurons receive STF top-down

connections whereas top-down projections onto pyramidal cells exhibit STD dynamics as required by our model [12–17]. In future work, it would be interesting to model the specific neuron types for each connection to satisfy Dale’s law and further increase biological plausibility.

A prediction from our model is that manipulations of these interneurons with STF connections would lead to disruptions in burst decoding from the layer (brain area) above thereby obstructing learning in the brain area below. Additionally, as error signals alter the level of bursting in the network, the model predicts that the variance in bursting activity and the distal dendritic potentials would correlate with the level of error in the network during learning.

Although our model captures a wide range of biological features, some biological implausibilities remain. Currently, we use feedback alignment to provide a solution to the *weight transport problem* [23] but this has a substantial impact on performance, particularly in more challenging tasks. Therefore, it would be important to explore some of the recently introduced plausible feedback learning rules [24–26] which could be used in conjunction with our proposed learning rules to outperform feedback alignment [4].

We have shown that our model can perform well with continuously varying input-output tasks. However, its membrane time constants impose limits on the speed at which information can be propagated forward and backward. Recent work has proposed a potential solution to this, termed *prospective coding*, which involves using predictive neuronal dynamics [27]. Alternatively, it has been proposed that the cerebellum predicts error signals which enables learning before the errors have fully propagated through the network [28, 29].

Overall, our work provides a novel solution to the credit assignment problem and suggests that a range of cortical features from sub-cellular to the systems level jointly underlie single-phase, efficient deep learning in the brain.

## **Acknowledgments and Disclosure of Funding**

The authors would like to thank Alexandre Payeur, Jordan Guerguiev, Kevin Nejad, Blake Richards, Richard Naud, Jesper Sjostrom, Paul Anastasiades, Joao Sacramento, Adil Khan and Jasper Poort for useful discussions. This work made use of the supercomputer BluePebble (BP). We would also like to thank Callum Wright and the rest of the High Performance Computing team at the University of Bristol for constant and quick help with BP. This work has been supported by two EPSRC Doctoral Training Partnership PhD studentships to WG and JP and a Wellcome Trust Neural Dynamics PhD studentship to HZ.

## References

- [1] Pieter R Roelfsema and Anthony Holtmaat. Control of synaptic plasticity in deep cortical networks. *Nature Reviews Neuroscience*, 19(3):166–180, 2018.
- [2] Blake A Richards, Timothy P Lillicrap, Philippe Beaudoin, Yoshua Bengio, Rafal Bogacz, Amelia Christensen, Claudia Clopath, Rui Ponte Costa, Archy de Berker, Surya Ganguli, et al. A deep learning framework for neuroscience. *Nature neuroscience*, 22(11):1761–1770, 2019.
- [3] Timothy P Lillicrap, Adam Santoro, Luke Marris, Colin J Akerman, and Geoffrey Hinton. Backpropagation and the brain. *Nature Reviews Neuroscience*, 21(6):335–346, 2020.
- [4] Timothy P Lillicrap, Daniel Cownden, Douglas B Tweed, and Colin J Akerman. Random synaptic feedback weights support error backpropagation for deep learning. *Nature communications*, 7(1):1–10, 2016.
- [5] Blake A Richards and Timothy P Lillicrap. Dendritic solutions to the credit assignment problem. *Current opinion in neurobiology*, 54:28–36, 2019.
- [6] João Sacramento, Rui Ponte Costa, Yoshua Bengio, and Walter Senn. Dendritic cortical microcircuits approximate the backpropagation algorithm. In *Advances in Neural Information Processing Systems*, pages 8721–8732, 2018.
- [7] Stephen R Williams and Greg J Stuart. Dependence of epsp efficacy on synapse location in neocortical pyramidal neurons. *Science*, 295(5561):1907–1910, 2002.
- [8] Ning-long Xu, Mark T Harnett, Stephen R Williams, Daniel Huber, Daniel H O’Connor, Karel Svoboda, and Jeffrey C Magee. Nonlinear dendritic integration of sensory and motor input during an active sensing task. *Nature*, 492(7428):247–251, 2012.
- [9] P Jesper Sjostrom, Ede A Rancz, Arnd Roth, and Michael Hausser. Dendritic excitability and synaptic plasticity. *Physiological reviews*, 88(2):769–840, 2008.
- [10] Alexandre Payeur, Jordan Guerguiev, Friedemann Zenke, Blake A Richards, and Richard Naud. Burst-dependent synaptic plasticity can coordinate learning in hierarchical circuits. *Nature neuroscience*, 24(7):1010–1019, 2021.
- [11] Richard Naud and Henning Sprekeler. Sparse bursts optimize information transmission in a multiplexed neural code. *Proceedings of the National Academy of Sciences*, 115(27):E6329–E6338, 2018.
- [12] Soohyun Lee, Ilya Kruglikov, Z Josh Huang, Gord Fishell, and Bernardo Rudy. A disinhibitory circuit mediates motor integration in the somatosensory cortex. *Nature neuroscience*, 16(11):1662–1670, 2013.
- [13] Amanda K Kinnischtzke, Daniel J Simons, and Erika E Fanselow. Motor cortex broadly engages excitatory and inhibitory neurons in somatosensory barrel cortex. *Cerebral cortex*, 24(8):2237–2248, 2014.
- [14] Iraklis Petrof, Angela N Viaene, and S Murray Sherman. Properties of the primary somatosensory cortex projection to the primary motor cortex in the mouse. *Journal of neurophysiology*, 113(7):2400–2407, 2015.
- [15] Timothy A Zolnik, Julia Ledderose, Maria Toumazou, Thorsten Trimbuch, Tess Oram, Christian Rosenmund, Britta J Eickholt, Robert NS Sachdev, and Matthew E Larkum. Layer 6b is driven by intracortical long-range projection neurons. *Cell reports*, 30(10):3492–3505, 2020.
- [16] Shovan Naskar, Jia Qi, Francisco Pereira, Charles R Gerfen, and Soohyun Lee. Cell-type-specific recruitment of gabaergic interneurons in the primary somatosensory cortex by long-range inputs. *Cell reports*, 34(8):108774, 2021.
- [17] Luis E Martinetti, Kelly E Bonekamp, Dawn M Autio, Hye-Hyun Kim, and Shane R Crandall. Short-term facilitation of long-range corticocortical synapses revealed by selective optical stimulation. *Cerebral cortex*, 32(9):1932–1949, 2022.

- [18] Elie L Bienenstock, Leon N Cooper, and Paul W Munro. Theory for the development of neuron selectivity: orientation specificity and binocular interaction in visual cortex. *Journal of Neuroscience*, 2(1):32–48, 1982.
- [19] Per Jesper Sjöström, Gina G Turrigiano, and Sacha B Nelson. Rate, timing, and cooperativity jointly determine cortical synaptic plasticity. *Neuron*, 32(6):1149–1164, 2001.
- [20] Tim P Vogels, Henning Sprekeler, Friedemann Zenke, Claudia Clopath, and Wulfram Gerstner. Inhibitory plasticity balances excitation and inhibition in sensory pathways and memory networks. *Science*, 334(6062):1569–1573, 2011.
- [21] Yann LeCun and Corinna Cortes. MNIST handwritten digit database. 2010. URL <http://yann.lecun.com/exdb/mnist/>.
- [22] Alex Krizhevsky, Vinod Nair, and Geoffrey Hinton. Cifar-10 (canadian institute for advanced research). URL <http://www.cs.toronto.edu/~kriz/cifar.html>.
- [23] Francis Crick. The recent excitement about neural networks. *Nature*, 337(6203):129–132, 1989.
- [24] Dong-Hyun Lee, Saizheng Zhang, Asja Fischer, and Yoshua Bengio. Difference target propagation. In *Joint european conference on machine learning and knowledge discovery in databases*, pages 498–515. Springer, 2015.
- [25] Mohamed Akrouf, Collin Wilson, Peter C Humphreys, Timothy Lillicrap, and Douglas Tweed. Using weight mirrors to improve feedback alignment. *arXiv preprint arXiv:1904.05391*, 2019.
- [26] Nasir Ahmad, Marcel A van Gerven, and Luca Ambrogioni. Gait-prop: A biologically plausible learning rule derived from backpropagation of error. *Advances in Neural Information Processing Systems*, 33:10913–10923, 2020.
- [27] Paul Haider, Benjamin Ellenberger, Laura Kriener, Jakob Jordan, Walter Senn, and Mihai A Petrovici. Latent equilibrium: A unified learning theory for arbitrarily fast computation with arbitrarily slow neurons. *Advances in Neural Information Processing Systems*, 34:17839–17851, 2021.
- [28] Joseph Pemberton, Ellen Boven, Richard Apps, and Rui Ponte Costa. Cortico-cerebellar networks as decoupling neural interfaces. *Advances in Neural Information Processing Systems*, 34, 2021.
- [29] Ellen Boven, Joseph Pemberton, Paul Chadderton, Richard Apps, and Rui Ponte Costa. Cerebro-cerebellar networks facilitate learning through feedback decoupling. *bioRxiv*, 2022.
- [30] Jordan Guerguiev, Timothy P Lillicrap, and Blake A Richards. Towards deep learning with segregated dendrites. *ELife*, 6:e22901, 2017.
- [31] Richard Naud, Nicolas Marcille, Claudia Clopath, and Wulfram Gerstner. Firing patterns in the adaptive exponential integrate-and-fire model. *Biological cybernetics*, 99(4):335–347, 2008.
- [32] Friedemann Zenke and Wulfram Gerstner. Limits to high-speed simulations of spiking neural networks using general-purpose computers. *Frontiers in neuroinformatics*, 8:76, 2014.
- [33] Lukas Biewald. Experiment tracking with weights and biases, 2020. URL <https://www.wandb.com/>. Software available from wandb.com.
- [34] Chiayu Q Chiu, James S Martenson, Maya Yamazaki, Rie Natsume, Kenji Sakimura, Susumu Tomita, Steven J Tavalin, and Michael J Higley. Input-specific nmdar-dependent potentiation of dendritic gabaergic inhibition. *Neuron*, 97(2):368–377, 2018.

## Supplementary Material

### A Model details

#### A.1 Continuous-time BurstCCN

In contrast to the discrete-time implementation, the continuous-time BurstCCN does not process each input example separately from one another. The network dynamics instead evolve through a continuous-time simulation incrementing with timesteps of  $dt = 0.1s$ , where there is a memory of the prior network state at each timestep and no parallel processing of mini-batches. The signals into the input layer are now given by a time-varying function,  $\mathbf{x}(t)$ , along with target signals to the output layer,  $\mathbf{y}(t)$ . The input layer event rate is set instantaneously as  $\mathbf{e}_0(t) = \mathbf{x}(t)$ . All somatic potentials and other layer event rates evolve with:

$$\frac{d\mathbf{v}_l(t)}{dt} = \frac{1}{\tau_v} \left( -\mathbf{v}_l(t) + \mathbf{W}_l(t)\mathbf{e}_{l-1}(t) \right) \quad (6)$$

$$\mathbf{e}_l(t) = f(\mathbf{v}_l(t)) \quad (7)$$

where  $\tau_v$  is the membrane leak time constant of the soma. The output layer burst probabilities are also set instantaneously as  $\mathbf{p}_L(t) = \mathbf{p}_L^b + \mathbf{p}_L^b \odot (\mathbf{y}(t) - \mathbf{e}_L(t)) \odot h(\mathbf{e}_l(t))$ . The hidden layer dendritic potentials, burst probabilities and burst rates evolve with:

$$\frac{d\mathbf{u}_l(t)}{dt} = \frac{1}{\tau_u} \left( -\mathbf{u}_l(t) + h(\mathbf{e}_l(t)) \odot \left[ \mathbf{Q}_l(t)\mathbf{e}_{l+1}(t) - \mathbf{Y}_l(t)\mathbf{b}_{l+1}(t) \right] \right) \quad (8)$$

$$\mathbf{p}_l(t) = \sigma(\mathbf{u}_l(t)) \quad (9)$$

$$\mathbf{b}_l(t) = \mathbf{p}_l(t) \odot \mathbf{e}_l(t) \quad (10)$$

where  $\tau_u$  is the membrane leak time constant of the apical dendrite. Finally, the feedforward weights change over time following:

$$\frac{d\mathbf{W}_l(t)}{dt} = \frac{1}{\tau_W} \left( \left[ \mathbf{p}_l(t) - \mathbf{p}_l^b \right] \odot \mathbf{e}_l(t) \right) \mathbf{e}_{l-1}^T(t) \quad (11)$$

where  $\tau_W$  is a time constant that determines the learning rate.

#### A.2 Spiking BurstCCN

Previous backprop-like learning models rely on computations across distinct phases to obtain the necessary error signals to learn [10, 30]. For example, Burstprop, proposed by Payeur et al. [10], computes the difference between the level of bursting between two phases: an initial phase with no teaching signal and a second with a teaching signal present. The burst-dependent plasticity rule used in the spiking implementation of Burstprop requires neuron ensembles to compute a moving average of their burst probability over time. This quantity needs to reach stability in order to generate useful error signals. Therefore, there must be a period with no plasticity before a teaching signal is presented. This requires global plasticity switches between the two phases which is problematic because a high level of coordinated plasticity is needed across the whole network. To address these issues, we build upon Burstprop's plasticity rule and propose a spiking implementation of our rate-based burst-dependent plasticity rule (Eq. 1):

$$\frac{dw_{ij}}{dt} = \eta \left[ B_i(t) - P_i^b E_i(t) \right] \tilde{E}_j(t) \quad (12)$$

where  $P^b$  is the baseline burst probability,  $\tilde{E}$  is an eligibility trace of presynaptic activity (with time constant  $\tau_{pre}$ ),  $\eta$  is a learning rate and  $B_i$  and  $E_i$  are burst and event trains, respectively. In contrast to Burstprop, we use a constant baseline burst probability instead of a moving average of the burst probability to control the relative magnitude of positive and negative weight changes. This makes it unnecessary to have a separate phase to compute its value since it is no longer time-dependent. However, to make single phase learning possible, we have also introduced a set of STD feedback weights that cancel bursting feedback activity into the apical compartments such that burst probabilities are restored to baseline. With just STF feedback weights, as is the case for Burstprop, it is not possible for cells to consistently burst at baseline in the absence of a teaching signal. This is

due to the bursting signals they communicate having a dependence on the feedforward activity (i.e. events) and necessarily varying across input stimuli.

We include this spike-based burst-dependent synaptic plasticity rule in a spiking implementation of the BurstCCN. Unlike the two rate-based implementations, the spiking BurstCCN more accurately models the internal neuron spiking dynamics instead of abstracting these details away and only considering the ensemble-level behaviour. Pyramidal neurons are modelled with two compartments corresponding to the soma and apical dendrites. Additionally, we modelled two different inhibitory interneuron populations (dendrite-targeting and perisomatic) using the adaptive exponential integrate and fire model [31] to provide inhibition. The remaining details of this model along with the hyperparameters used are described by Payeur et al. [10] and the simulation of all neurons was carried out using the Auryn simulator [32].

## B BurstCNN approximates the backpropagation algorithm

In Section 3.3.1, we discussed the relationship between BurstCNN and the error backpropagation algorithm. Here, we demonstrate their relationship formally and specify the constraints required for an equivalence.

We first remind the reader of the process of error backpropagation. Using the notation of the main text and letting  $\mathbf{g}_l = \frac{\partial E^{\text{task}}}{\partial \mathbf{v}_l}$  denote the error gradient with respect to the somatic potentials at layer  $l$ , the error backpropagation algorithm generates  $\mathbf{g}_l$  recursively with

$$\mathbf{g}_L = f'(\mathbf{v}_L) \odot \frac{\partial E^{\text{task}}}{\partial \mathbf{e}_L} \quad (13)$$

$$\mathbf{g}_l = f'(\mathbf{v}_l) \odot \mathbf{W}_{l+1}^T \mathbf{g}_{l+1} \quad (14)$$

where  $f'$  denotes the first order derivative of  $f$ . The error gradients with respect to the feedforward weights onto layer  $l$  can then simply be obtained with  $\frac{\partial E^{\text{task}}}{\partial \mathbf{W}_l} = \frac{\partial E^{\text{task}}}{\partial \mathbf{v}_l} \left( \frac{\partial \mathbf{v}_l}{\partial \mathbf{W}_l} \right)^T = \mathbf{g}_l \mathbf{e}_{l-1}^T$ .

To demonstrate an equivalence of the weight updates obtained by BurstCNN (Eq. 1) with those of error backpropagation, it is necessary to show that the difference between the burst rate and its baseline  $\delta \mathbf{b}_l := (\mathbf{p}_l - \mathbf{p}_l^b) \odot \mathbf{e}_l$  mirrors the quantity  $-\mathbf{g}_l$ . Note that by construction this is true (up to the proportionality constant  $p_l^b$ ) for the output layer  $L$  since

$$\begin{aligned} \delta \mathbf{b}_L &= \mathbf{p}_L^b \odot (\mathbf{e}_{\text{target}} - \mathbf{e}_L) \odot h(\mathbf{e}_L) \odot \mathbf{e}_L \\ &= p_L^b f'(\mathbf{v}_L) \odot (\mathbf{e}_{\text{target}} - \mathbf{e}_L) \\ &= p_L^b f'(\mathbf{v}_L) \odot \left( -\frac{\partial E^{\text{task}}}{\partial \mathbf{e}_L} \right) \\ &= -p_L^b \mathbf{g}_L. \end{aligned}$$

To demonstrate that  $\delta \mathbf{b}_l \approx -p_l^b \mathbf{g}_l$  for layers  $l < L$  it is then left to show that  $\delta \mathbf{b}_l$  satisfies the recursive relationship in Equation 14. For reasons which will become apparent we proceed under the assumption of the  $\mathbf{Q}$ - $\mathbf{Y}$  symmetric state,  $\mathbf{Q}_l = p_l^b \mathbf{Y}_l$  under the particular case that  $p_l^b = \frac{1}{2}$  for each layer  $l$ . By applying the definition of  $\delta \mathbf{b}_l$  and expanding the sigmoid term in the burst probability  $\mathbf{p}_l$  by its Taylor series,  $\sigma(x) = \frac{1}{2} + \frac{x}{4} + \frac{x^3}{48} + \dots$ , we obtain

$$\begin{aligned}
\delta \mathbf{b}_l &= (\mathbf{p}_l - p_l^b) \odot \mathbf{e}_l \\
&= \left(\mathbf{p}_l - \frac{1}{2}\right) \odot \mathbf{e}_l \\
&= \mathbf{p}_l \odot \mathbf{e}_l - \frac{1}{2}\mathbf{e}_l \\
&= \left(\bar{\sigma}(h(\mathbf{e}_l) \odot \mathbf{u}_l)\right) \odot \mathbf{e}_l - \frac{1}{2}\mathbf{e}_l \\
&= \left(\sigma(4h(\mathbf{e}_l) \odot \mathbf{u}_l)\right) \odot \mathbf{e}_l - \frac{1}{2}\mathbf{e}_l \\
&= \left(\frac{1}{2} + \frac{4h(\mathbf{e}_l) \odot \mathbf{u}_l}{4} + \mathcal{O}(\mathbf{u}_l^3)\right) \odot \mathbf{e}_l - \frac{1}{2}\mathbf{e}_l \\
&= \frac{1}{2}\mathbf{e}_l + h(\mathbf{e}_l) \odot \mathbf{u}_l \odot \mathbf{e}_l + \mathcal{O}(\mathbf{u}_l^3) - \frac{1}{2}\mathbf{e}_l \\
&= h(\mathbf{e}_l) \odot (\mathbf{Q}_l \mathbf{e}_{l+1} - \mathbf{Y}_l \mathbf{b}_{l+1}) \odot \mathbf{e}_l + \mathcal{O}(\mathbf{u}_l^3) \\
&= h(\mathbf{e}_l) \odot \left(\frac{\mathbf{Y}_l}{2} \mathbf{e}_{l+1} - \mathbf{Y}_l \mathbf{b}_{l+1}\right) \odot \mathbf{e}_l + \mathcal{O}(\mathbf{u}_l^3) \\
&= h(\mathbf{e}_l) \odot \mathbf{e}_l \odot (-\mathbf{Y}_l) \left(\mathbf{b}_{l+1} - \frac{1}{2}\mathbf{e}_{l+1}\right) + \mathcal{O}(\mathbf{u}_l^3) \\
&= f'(\mathbf{v}_l) \odot (-\mathbf{Y}_l) \left(\left(\mathbf{p}_{l+1} - \frac{1}{2}\right) \odot \mathbf{e}_{l+1}\right) + \mathcal{O}(\mathbf{u}_l^3) \\
&= f'(\mathbf{v}_l) \odot (-\mathbf{Y}_l) \left((\mathbf{p}_{l+1} - p_{l+1}^b) \odot \mathbf{e}_{l+1}\right) + \mathcal{O}(\mathbf{u}_l^3) \\
&= f'(\mathbf{v}_l) \odot (-\mathbf{Y}_l) \delta \mathbf{b}_{l+1} + \mathcal{O}(\mathbf{u}_l^3).
\end{aligned}$$

Here, we use the abuse of notation  $\mathbf{u}_l^3 = (u_{l,1}^3, u_{l,2}^3, \dots)^T$  and apply the Taylor series expansion under the assumptions that the apical potential is bounded by 1,  $\|\mathbf{u}_l\|_\infty \leq 1$  (so that the cube term dominates), and that  $h$  is bounded (so that the expanded term  $h(\mathbf{e}_l) \odot \mathbf{u}_l^3$  is of order  $\mathcal{O}(\mathbf{u}_l^3)$ ). Note that for the sigmoid forward activation  $f = \sigma$  the latter is satisfied automatically since  $h(\mathbf{e}_l) = 1 - \mathbf{e}_l$  with  $\mathbf{e}_l$  itself bounded (between 0 and 1). The above derivation then leads to the result cited in the main text (Eq. 3). In particular, if the apical potential is small enough such that  $\mathcal{O}(\mathbf{u}_l^3) \approx 0$  and the  $\mathbf{W}$  and  $\mathbf{Y}$  weights are aligned with  $\mathbf{Y}_l = -\mathbf{W}_{l+1}^T$ , we have an equivalence to the error backpropagation algorithm of Equation 14:

$$\delta \mathbf{b}_l \approx f'(\mathbf{v}_l) \odot \mathbf{W}_{l+1}^T \delta \mathbf{b}_{l+1} \quad (15)$$

## B.1 Backpropagation of apical potentials

In this section, we show that the approximation error in Equation 3, specifically the Euclidean norm of its cube,  $\|\mathbf{u}_l^3\|_2$ , remains small across all layers if it is small at the output layer and the feedback weights are weak. This can be shown through induction by first assuming that layer  $l+1$  has small enough apical potentials such that  $\mathcal{O}(\mathbf{u}_{l+1}^3) \approx 0$  (i.e. it is in the linear regime of  $\sigma$ ). We again assume to be in the  $\mathbf{Q}$ - $\mathbf{Y}$  symmetric state  $\mathbf{Q}_l = \frac{\mathbf{Y}_l}{2}$ . The apical potential at the preceding layer  $l$  can then be written as

$$\begin{aligned}
\mathbf{u}_l &= \mathbf{Q}_l \mathbf{e}_{l+1} - \mathbf{Y}_l \mathbf{b}_{l+1} \\
&= \frac{\mathbf{Y}_l}{2} \mathbf{e}_{l+1} - \mathbf{Y}_l (\sigma(4h(\mathbf{e}_{l+1}) \odot \mathbf{u}_{l+1}) \odot \mathbf{e}_{l+1}) \\
&= \frac{\mathbf{Y}_l}{2} \mathbf{e}_{l+1} - \mathbf{Y}_l \left( \left( h(\mathbf{e}_{l+1}) \odot \mathbf{u}_{l+1} + \frac{1}{2} \right) \odot \mathbf{e}_{l+1} \right) \\
&= \frac{\mathbf{Y}_l}{2} \mathbf{e}_{l+1} - \mathbf{Y}_l h(\mathbf{e}_{l+1}) \odot \mathbf{u}_{l+1} \odot \mathbf{e}_{l+1} - \frac{\mathbf{Y}_l}{2} \mathbf{e}_{l+1} \\
&= (-\mathbf{Y}_l) (h(\mathbf{e}_{l+1}) \odot \mathbf{e}_{l+1} \odot \mathbf{u}_{l+1}) \\
&= (-\mathbf{Y}_l) (f'(\mathbf{v}_{l+1}) \odot \mathbf{u}_{l+1}).
\end{aligned}$$

Intuitively, given that  $f'$  is bounded by 1 (as is the case for ReLU, sigmoid and tanh), we only require that the feedback weights  $\mathbf{Y}_l$  (or equivalently the forward weights  $\mathbf{W}_l$  in the  $\mathbf{W}$ - $\mathbf{Y}$  symmetric state) are small enough such that the final term above is less than or equal to the apical potentials in the next layer,  $\mathbf{u}_{l+1}$ . In fact, to formally ensure that the size of the approximation error in Equation 3 shrinks layer by layer, i.e.  $\|\mathcal{O}(\mathbf{u}_l^3)\|_2 \leq \|\mathcal{O}(\mathbf{u}_{l+1}^3)\|_2$ , we can enforce the condition that the 6-norm of the feedback weights  $\mathbf{Y}_l$  is at most 1; that is,  $\|\mathbf{Y}_l\|_6 = \sup_{\mathbf{x} \neq 0} \frac{\|\mathbf{Y}_l \mathbf{x}\|_6}{\|\mathbf{x}\|_6} \leq 1$ . With this we have

$$\begin{aligned}
\|\mathbf{u}_l^3\|_2 &= \|\mathbf{u}_l^3\|_2 \\
&= (\|\mathbf{u}_l\|_6)^3 \\
&= (\|\mathbf{Y}_l (f'(\mathbf{v}_{l+1}) \odot \mathbf{u}_{l+1})\|_6)^3 \\
&\leq (\|f'(\mathbf{v}_{l+1}) \odot \mathbf{u}_{l+1}\|_6)^3 \\
&= (\|\mathbf{u}_{l+1}\|_6)^3 \\
&= \|\mathbf{u}_{l+1}^3\|_2.
\end{aligned}$$

Hence we have the approximation error in Equation 3 at layer  $l$  less than or equal to the approximation error at layer  $l+1$ ,  $\|\mathcal{O}(\mathbf{u}_l^3)\|_2 \leq \|\mathcal{O}(\mathbf{u}_{l+1}^3)\|_2$ . Finally, we note that the uppermost defined apical potentials (at layer  $L-1$ ) can be derived as

$$\begin{aligned}
\mathbf{u}_{L-1} &= \mathbf{Q}_{L-1} \mathbf{e}_L - \mathbf{Y}_{L-1} \mathbf{b}_L \\
&= \frac{\mathbf{Y}_{L-1}}{2} \mathbf{e}_L - \mathbf{Y}_{L-1} \left( \frac{1}{2} \mathbf{e}_L - \frac{1}{2} h(\mathbf{e}_L) \odot \mathbf{e}_L \odot \frac{\partial E^{\text{task}}}{\partial \mathbf{e}_L} \right) \\
&= f'(\mathbf{v}_L) \odot (-\mathbf{Y}_{L-1}) \left( -\frac{1}{2} \frac{\partial E^{\text{task}}}{\partial \mathbf{e}_L} \right).
\end{aligned}$$

Although it is not explicitly defined in the BurstCCN, we can think of the apical potentials at the final layer  $L$  as (at least computationally equivalent to)  $-\frac{1}{2} \frac{\partial E^{\text{task}}}{\partial \mathbf{e}_N}$ . If these are appropriately small, then by induction, all apical potentials of the lower layers  $\mathbf{u}_{1 \leq l \leq L-1}$  will be appropriately small such that we have  $\delta \mathbf{b}_l \approx -\frac{1}{2} \mathbf{g}_l$  for each  $l$  and an equivalence to the weight updates defined in backpropagation (Equations 4, 5).

**Case where  $p_l^b \neq \frac{1}{2}$**

Note that for  $p_l^b \neq \frac{1}{2}$ , a similar derivation as in Equation 3 can be made by applying an offset  $\beta$  to the sigmoid  $\bar{\sigma}(x) = \sigma(4 \cdot x + 4\beta)$  where  $\beta = p_l^b - \frac{1}{2}$ , in order to linearise the function around  $-\beta$ . However, this introduces an extra error term in the approximation which scales with  $|p_l^b - \frac{1}{2}|$  and makes very high or low baseline burst probabilities undesirable.



## B.2 Local plasticity rules ensure Q-Y symmetry in absence of teaching signal

We now show that the local update rule for the STD feedback weights,  $\mathbf{Q}$ , as defined in Equation 2, leads to the Q-Y symmetric state as required in the sections above. In particular, we show that in the absence of an explicit teaching signal at the output layer and assuming independent somatic potentials in the population,  $\mathbf{Q}_l$  will converge onto the solution  $\mathbf{Q}_l = p_l^b \mathbf{Y}_l$ .

First, we note that Equation 2 is simply implementing gradient descent with respect to the size of the apical potential  $\|\mathbf{u}_l\|_2$ .

$$\Delta \mathbf{Q}_l \propto -\frac{\partial \|\mathbf{u}_l\|_2^2}{\partial \mathbf{Q}_l} = -\frac{\partial \|\mathbf{Q}_l \mathbf{e}_{l+1} - \mathbf{Y}_l \mathbf{b}_{l+1}\|_2^2}{\partial \mathbf{Q}_l} = -(\mathbf{Q}_l \mathbf{e}_{l+1} - \mathbf{Y}_l \mathbf{b}_{l+1}) \mathbf{e}_{l+1}^T = -\mathbf{u}_l \mathbf{e}_{l+1}^T \quad (16)$$

Following this gradient (with appropriate learning rate  $\eta_l^{(\mathbf{Q})}$ ) should therefore ensure reaching a local minimum on  $\|\mathbf{u}_l\|_2$ . However, since this is simply a (linear) least squares regression problem, the function  $\phi : \mathbf{Q} \rightarrow \|\mathbf{u}_l\|_2^2$  is convex and therefore any local minimum is the global minimum.

To show that  $\mathbf{Q}_l$  will converge onto  $p_l^b \mathbf{Y}_l$  itself (rather than another solution), we see that, in the absence of a teaching signal, this solution enforces  $\mathbf{u}_l = 0$ .

$$\mathbf{u}_l = \mathbf{Q}_l \mathbf{e}_{l+1} - \mathbf{Y}_l \mathbf{b}_{l+1} = p_l^b \mathbf{Y}_l \mathbf{e}_{l+1} - p_l^b \mathbf{Y}_l \mathbf{e}_{l+1} = 0 \quad (17)$$

Thus,  $\mathbf{Q}_l = p_l^b \mathbf{Y}_l$  achieves the global minimum  $\|\mathbf{u}_l\|_2^2 = \|0\|_2^2 = 0$ . Moreover, in the case that the event rates  $\mathbf{e}_{l+1}$  are linearly independent, we have  $\mathbf{Q}_l = p_l^b \mathbf{Y}_l$  as the unique solution. Although linear independence of  $\mathbf{e}_{l+1}$  is not assured a priori, this can be guaranteed, for example, by independently injecting noise current into the population (see Section C.3.2). The (global) minimum obtained by the update rules in Equation 2 must therefore correspond to this solution  $\mathbf{Q}_l = p_l^b \mathbf{Y}_l$ , ensuring Q-Y symmetry as required.

## C Experimental details

In the following section, we provide additional details on the experimental setup used to obtain the results in the main text.

### C.1 Spiking XOR task

In the spiking XOR task, we used networks consisting of 5 distinct neuron populations: 2 populations that encoded each input, 2 hidden layer populations and a single population that encoded the output. Each population consisted of 500 individual neurons. These neurons were sparsely connected in the feedforward and feedback directions with a connection probability of 0.05. All neurons received balanced excitatory and inhibitory Poisson noise into both their somatic and dendritic compartments.

In the two-phase setup, learning rates for the weights and biases were set to  $\eta_W = 0.004$  and  $\eta_B = 0.0001$ , respectively. We reduced learning rates to  $\eta_W = 0.0004$  and  $\eta_B = 0.00001$  in the one-phase setup due to the increased duration where plasticity was on.

Each simulation was carried out for 16000s (2000 examples  $\times$  8s per example) with timesteps of  $dt = 0.1s$ . Learning of the feedforward weights was carried out by each model's burst-dependent synaptic plasticity rule with the time constant of the pre-synaptic input eligibility trace  $\tau_{pre} = 0.1s$ . The moving average time constant for Burstprop,  $\tau_{ma}$  was set to 2s. Baseline burst probabilities in the BurstCCN were set to  $P_{hidden}^b = 0.18$  and  $P_{out}^b = 0.401$  in the hidden and output layers, respectively. The remaining task details can be found in [10].

### C.2 Continuous-time input-output task

This task was carried out using a 2-layer continuous-time BurstCCN with 3 inputs, 50 hidden units and a single output unit. The simulation was ran for  $10^6$  timesteps with  $dt = 0.1s$  to give a total simulation time of  $10^5s$ . During the first 100s of the simulation, plasticity and teaching signals

were switched off to provide a means of comparing the initialised network to the trained network (Fig. 3C-D). The time constants used in the simulation for the somatic potentials, dendritic potentials and the synaptic weights were set to  $\tau_v = 0.1s$ ,  $\tau_u = 0.1s$  and  $\tau_W = 100.0s$ , respectively.

### C.3 Rate-based model experiments

#### C.3.1 Hyperparameter search

Bayesian hyperparameter optimisation was performed (using Weights & Biases [33]) for the shared hyperparameters of each rate-based model shown in Tables S1-S2 and S4-S5. This was also performed for the model-specific parameters that are stated in the following relevant sections.

#### C.3.2 Feedback plasticity on Q weights

As described in Section 3.3.2, this task involved fixing the **W** and **Y** weights and allowing the **Q** weights to learn following the plasticity rule given in Equation 2. Throughout training, independent Gaussian noise was added to the event rates propagating forwards to give somatic potentials,  $\mathbf{v}_l = \mathbf{W}_l(\mathbf{e}_{l-1} + \xi)$  where  $\xi \sim \mathcal{N}(\mathbf{0}, \sigma^2 \mathbf{I})$ . This noise was introduced to decorrelate neural activities in each layer to facilitate the alignment of **Q** to **Y** (see Section B.2). For all configurations, we set  $\sigma = 0.1$  during training but removed the noise when evaluating the apical potential magnitudes (Fig. 4B,F) and alignment angles (Fig.4C-D,G-H). Similarly, in the without-teacher setups, teaching signals were added only for the evaluation of the alignment angles to backprop or feedback alignment. Table S1 shows the best hyperparameters for each setup optimised for **Q-Y** alignment.

Table S1: Q-weight learning hyperparameters

Feedback mode	Teacher	Q learning rate ( $\eta^{(Q)}$ )	Y init. scale ( $\sigma_Y$ )	Q init. scale ( $\sigma_Q$ )
Random (FA)	No	0.00520	0.5	0.0148
Symmetric	No	0.00337	N/A	0.00750
Random (FA)	Yes	0.00380	0.5	0.0488
Symmetric	Yes	0.00677	N/A	0.0735

#### C.3.3 MNIST

For MNIST, we used a standard ANN, BurstCCN, Burstprop and EDN model. The same network structure was used for all model types: 784 inputs ( $28 \times 28$  greyscale images),  $n$  number of hidden layers with 500 units and 10 output units. In all cases, we used a sigmoid for the feedforward activation functions and a batch size of 32. Table S2 shows the best hyperparameters found for the 5-layer networks of each model which were shared across all network sizes.

**BurstCCN** The additional **Q** weights were trained with a learning rate of  $3.5 \times 10^{-5}$  and the baseline burst probability  $\mathbf{p}_l^b = 0.5$  for all layers.

**Burstprop** The additional recurrent weights were initialised from a Gaussian distribution (with  $\mu = 0$  and  $\sigma = 1.3 \times 10^{-4}$ ) and trained with a learning rate of  $2.6 \times 10^{-4}$ . The baseline burst probability at the output layer was set to 0.2.

**EDN** Learning rates for the interneuron-to-pyramidal ( $\eta_{l,l}^{PI}$ ) and pyramidal-to-interneuron ( $\eta_{l,l}^{IP}$ ) weights were set proportionally to the feedforward learning rates ( $\eta_{l+1,l}^{PP}$ ) as  $\eta_{l,l}^{PI} = \eta_{l,l}^{IP} = \alpha \eta_{l+1,l}^{PP}$  with the proportionality constant  $\alpha = 0.643$ .

#### C.3.4 CIFAR-10

For CIFAR-10, we used a standard ANN, BurstCCN and Burstprop model. We used a convolutional neural network with three convolutional layers followed by two fully-connected layers (Table S3). In all cases, we used a sigmoid for the feedforward activation functions and a batch size of 32. Table S4 and Table S5 show the best hyperparameters shared across the different models in the random fixed **Y** and **W-Y** symmetric feedback weight regimes, respectively.

Table S2: MNIST hyperparameters

Model Type	Learning rate ( $\eta$ )	Y init. scale ( $\sigma_Y$ )	Momentum	Weight decay
ANN	0.201	1.49	0.474	$1.09 \times 10^{-9}$
BurstCCN	0.0246	0.638	0.836	$4.01 \times 10^{-10}$
BurstCCN (Q-Y sym)	0.0246	0.638	0.836	$4.01 \times 10^{-10}$
Burstprop	0.481	1.71	0.347	$7.59 \times 10^{-6}$
EDN	0.00578	2.60	0.198	$2.01 \times 10^{-7}$

**BurstCCN** The additional **Q** weights were trained with a learning rate of  $2.21 \times 10^{-3}$  and the baseline burst probability  $p_i^b = 0.5$  for all layers.

**Burstprop** Under the random fixed **Y** feedback weight regime, the additional recurrent weights were initialised from a Gaussian distribution (with  $\mu = 0$  and  $\sigma = 2.0 \times 10^{-4}$ ) and trained with a learning rate of  $2.0 \times 10^{-4}$ . Under the **W-Y** symmetric weight regime, the additional recurrent weights were initialised from a Gaussian distribution (with  $\mu = 0$  and  $\sigma = 2.5 \times 10^{-2}$ ) and trained with a learning rate of  $2.2 \times 10^{-5}$ . For both weight regimes, the baseline burst probability at the output layer was set to 0.2.

Table S3: CIFAR-10 architecture

Layer number	Layer type	Size
0	Input	$32 \times 32 \times 3$
1	Convolutional	$5 \times 5, 64, \text{stride}=2$
2	Convolutional	$5 \times 5, 128, \text{stride}=2$
3	Convolutional	$3 \times 3, 256, \text{stride}=1$
4	Fully-connected	1480 neurons
5	Fully-connected	10 neurons

Table S4: CIFAR-10 hyperparameters (random fixed **Y** feedback weight regime)

Model Type	Learning rate ( $\eta$ )	Y init. scale ( $\sigma_Y$ )	Momentum	Weight decay
ANN	0.00335	0.363	0.502	$5.96 \times 10^{-8}$
BurstCCN	0.0343	0.424	0.0142	$1.01 \times 10^{-10}$
BurstCCN (Q-Y sym)	0.0132	0.290	0.578	$2.65 \times 10^{-9}$
Burstprop	0.102	0.981	0.698	$3.91 \times 10^{-9}$

## D Additional experiments

Here we describe a set of additional experiments that we have conducted. The first demonstrates that the distal cancellation can also be performed by having plasticity on the **Y** weights. The second shows the results for MNIST in the **W-Y** symmetric regime which more closely resembles backprop. Finally, we use an idealised version of the EDN to highlight the cause of the EDN’s poor performance.

### D.1 Feedback plasticity on Y-weights

As stated in the main text, the feedback plasticity rule used on the **Q** weights, likewise, could be applied to the **Y** weights to produce a similar effect. This would be in line with long-term synaptic plasticity observations of dendrite-targeting interneurons [34].

$$\Delta \mathbf{Y}_l = \eta_l^{(Y)} \mathbf{u}_l \mathbf{e}_{l+1}^T \quad (18)$$

In an identical experimental setup to the one used for investigating the feedback plasticity rule on the **Q** weights (Section 3.3.2), we examined the impact on the alignment to backprop when the feedback plasticity rule was instead applied onto the **Y** weights. In all cases, as the alignment

Table S5: CIFAR-10 hyperparameters ( $W$ - $Y$  symmetric weight regime)

Model Type	Learning rate ( $\eta$ )	Momentum	Weight decay
ANN	0.0814	0.447	$1.60 \times 10^{-6}$
BurstCCN ( $Q$ - $Y$ sym)	0.155	0.496	$1.50 \times 10^{-8}$
Burstprop	0.146	0.869	$2.53 \times 10^{-8}$

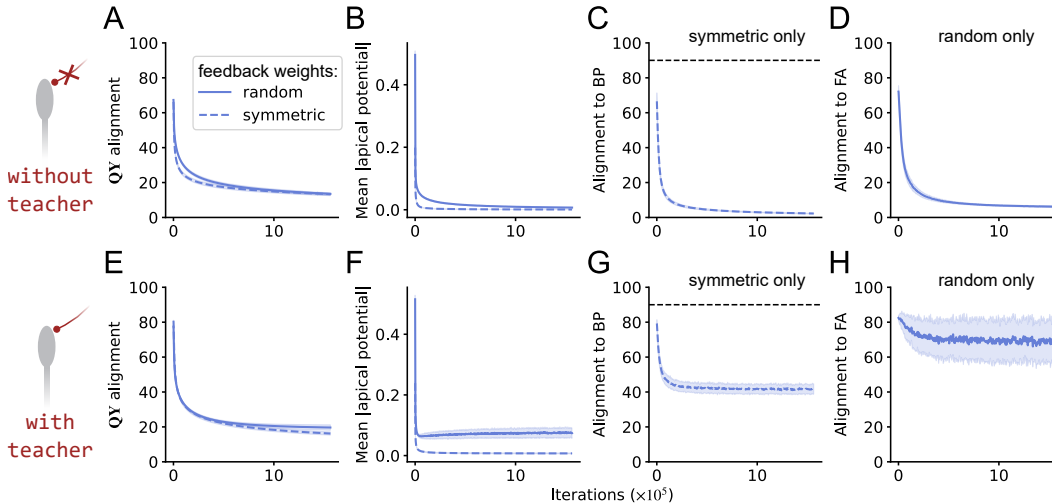


Figure S1: **Feedback plasticity rule on  $Y$  weights facilitates updates to align with backprop and feedback alignment.** The network is a randomly initialised 5-layer discrete-time BurstCCN with random (solid line) or symmetric (dashed line), fixed  $W$  and  $Y$  weights. The  $Y$  weights are updated in the presence of (A-D) no teaching signal or (E-H) a teaching signal. (A,E) Alignment between  $Q$  and  $Y$  connections, (B,F) the mean absolute value of the apical potentials, (C,G) the alignment to backprop (BP) and (D,H) feedback alignment (FA) as  $Y$  weights learn to silence apical dendrite potential. Updates below  $90^\circ$  marked by the black dashed line are considered useful as they still follow the direction to backprop on average. Model results represent mean  $\pm$  standard error ( $n = 5$ ).

between the  $Q$  and  $Y$  connections improved (Fig. S1A,E), the apical potential decreased (Fig. S1B,F) and this resulted in updates that more closely aligned to backprop (Fig. S1C,G) and feedback alignment (Fig. S1D,H). In the absence of a teaching signal, this alignment angle to both backprop and feedback alignment eventually became very small (Fig. S1C-D). Despite producing less aligned feedforward updates in the presence of a teaching signal, the updates computed were still informative since they were consistently well below  $90^\circ$  of the direction of steepest descent (Fig. S1G). Overall, this suggests that the feedback plasticity rule on the  $Q$  weights is equally effective when applied to the  $Y$  weights.

## D.2 Symmetric MNIST

Here, we trained the same models used in Figure 5 under the  $W$ - $Y$  symmetric weight regime. This regime is implausible due to sharing of weights but we investigated this to isolate the ability of each network to backpropagate errors in the ideal setting that most resembles backprop.

Using 5-layer networks, BurstCCN ( $Q$ - $Y$  sym) obtained a test error of  $1.86 \pm 0.03\%$  similar to that of an ANN ( $1.97 \pm 0.04\%$ ) and outperforming both Burstprop ( $2.79 \pm 0.03\%$ ) and EDN ( $12.28 \pm 0.26\%$ ) (Fig. S2A). However, the BurstCCN with  $Q$  weight learning achieved a performance of  $5.27 \pm 0.07\%$ . This was lower than the random fixed  $Y$  weight regime (Fig. 5) due to the increased difficulty of aligning with the rapidly moving  $Y$  weights as the network learns. As the network depth increased, both BurstCCN and Burstprop retained high performances but the EDN showed a substantial decay in performance with deeper networks (Fig. S2B). We then compared the alignment between the models and backprop. For the 5-layer networks, BurstCCN consistently produced updates that

aligned with backprop at around  $50^\circ$  (Fig. S2C). As expected, the BurstCCN with **Q-Y** symmetry was significantly better at propagating error signals. With increased network depths, we demonstrated that it was more difficult to produce updates that were closely aligned to backprop. However, we showed that the BurstCCN was still capable of backpropagating useful error signals in relatively deep networks (Fig. S2D).

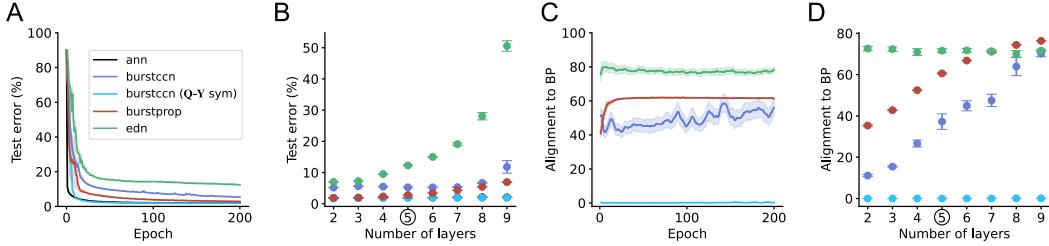


Figure S2: **BurstCCN with W-Y symmetric weights.** (A) Learning curve and (C) alignment to backprop of 5-layer BurstCCN (blue), BurstCCN ( $\eta^{(Q)} = 0$ ) (light blue), Burstprop (red) and EDN (green). (B) Different number of hidden layers across all models. (D) Alignment to backprop (BP) across number of hidden layers. The black circle indicates that the hyperparameters for each model were optimised for 5-layer networks. Model results represent mean  $\pm$  standard error ( $n = 5$ ).

### D.3 EDN with interneuron weight symmetry

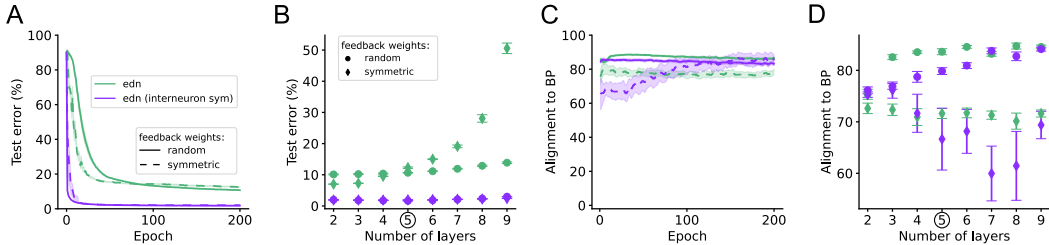


Figure S3: **EDN with interneuron symmetric weights.** (A) Learning curve and (C) alignment to backprop of 5-layer EDN (green) and EDN in the interneuron symmetric weight regime (purple) with random (solid) or symmetric (dashed) feedback weights. (B) Different number of hidden layers across all models. (D) Alignment to backprop (BP) across number of hidden layers. Circles and diamonds indicate the random and symmetric feedback weight regimes, respectively. The black circle indicates that the hyperparameters for each model were optimised for 5-layer networks. Model results represent mean  $\pm$  standard error ( $n = 5$ ).

Each layer in the EDN includes a set of apical-targeting interneurons which predict next layer activity and facilitate the generation of error signals for learning. These interneurons have lateral connections to and from pyramidal cells in the same layer. In the ideal case, the weights of the connections to and from these interneurons should exactly mirror the feedforward and feedback connections between the layers of pyramidal cells, respectively. We refer to this as the interneuron symmetric weight regime. This exact symmetry is not biologically plausible so the standard EDN model uses local plasticity rules for these connections to learn approximate symmetries.

Here, we evaluated the performance of a standard EDN model and an EDN model in the interneuron symmetric weight regime on MNIST. Using 5-layer networks, we show that the EDN in the interneuron symmetric weight regime (random:  $1.644 \pm 0.018\%$ , symmetric:  $1.962 \pm 0.019\%$ ) significantly outperformed the EDN (random:  $12.28 \pm 0.26\%$ , symmetric:  $10.65 \pm 0.09\%$ ) (Fig. S3A). This was irrespective of the feedback weight regime demonstrating the importance of the interneuron weight symmetry. As the network depth increased, the EDN, particularly in the symmetric weight regime, suffered a substantial reduction in performance. However, this large effect of depth on performance was less evident with the EDN under the interneuron symmetric weight regime (Fig. S3B). As expected, the alignment to backpropagation was closer with symmetric feedback weights compared to random fixed feedback weights (Fig. S3C-D).

## E Compute resources

The experiments involving the Aurn simulator were conducted with an AMD Ryzen 7 3700X CPU. For the different methods, we ran a total of 5 seeds which each took approximately 3 hours. The remaining experiments were conducted using NVIDIA GeForce RTX 2080 Ti GPUs. The runtime for each experiment per seed was approximately:

- **Continuous input-output task** - 50 minutes ( $10^6$  timesteps)
- **Q weight plasticity** - 6 hours (1000 epochs)
- **MNIST** - 50 minutes (200 epochs)
- **CIFAR-10** - 3 hours (400 epochs)

## F Code availability

The source code for this project can be found at <https://github.com/neuralml/BurstCCN>.